Mesoscale Convective Vortices Observed during BAMEX. Part I: Kinematic and Thermodynamic Structure

CHRISTOPHER A. DAVIS AND STANLEY B. TRIER

National Center for Atmospheric Research, Boulder, Colorado*

(Manuscript received 13 March 2006, in final form 19 September 2006)

ABSTRACT

Five cases of mesoscale convective vortices (MCVs) are described from observations collected during the Bow Echo and MCV Experiment (BAMEX) over the central United States during the period from 20 May to 6 July 2003. In the present paper, the kinematic and thermodynamic structure of each vortex and its environment are emphasized. Data consist of BAMEX dropsondes, the National Oceanic and Atmospheric Administration profiler network, and National Weather Service soundings. In addition, Weather Surveillance Radar-1988 Doppler observations documented the signatures of nascent MCVs within nocturnal convection systems as well as the spatial pattern of convection within MCVs during the following day. The vertical structure of each vortex was highly dependent on the vertical shear and the presence of upper-tropospheric cyclonic vorticity anomalies. In strong shear, a pronounced downshear tilt of the vortex was evident, but with the presence of an upper-tropospheric trough, the tilt was upshear in the upper troposphere. In only one case did the tangential velocity of the vortex greatly exceed the vertical shear across its depth, and thus the vortex could maintain itself against the shear. The vortices were generally deep structures, extending through 5–8 km in all cases and maximizing their tangential winds between 550 and 600 hPa. In one of the five cases, vertical penetration into the boundary layer was unambiguous. Lower-tropospheric virtual potential temperature anomalies were generally 1–2 K, greatest when not directly beneath the midtropospheric MCV center but rather on its upshear and downshear flanks. Upper-tropospheric warm anomalies were found above and downshear from the midtropospheric MCV center, with a cool anomaly upshear, the latter being stronger in cases with an upshear tropopause-based trough. A diagnostic balance calculation was performed and indicated that the temperature anomalies were approximately balanced on the scale of the vortex.

1. Introduction

One of the two primary objectives of the Bow Echo and Mesoscale Convective Vortex (MCV) Experiment (BAMEX) was to observe the spectrum of vortical structures believed to exist within mesoscale convective systems (MCSs) and to document their life cycle. The emphasis was on vortices with characteristic length scales between 50 and 200 km, although evidence for a broad spectrum of vortices within individual convection systems has been found (Wakimoto et al. 2006). The structure, climatology, and significance of mesoscale vortices induced by convection have been discussed in previous papers on the subject (Smull and Houze 1985; Zhang and Fritsch 1987; McAnelly and Cotton 1989; Menard and Fritsch 1989; Raymond and Jiang 1990; Bartels and Maddox 1991; Zhang 1992; Davis and Weisman 1994; Fritsch et al. 1994; Olsson and Cotton 1997; Trier et al. 2000b; Davis et al. 2002). These vortices have been hypothesized to initiate convection through quasi-balanced vertical motion in sheared flows (Raymond and Jiang 1990), providing a feedback to vortex intensity that can result in a diurnal oscillation between convection and unbalanced motion (night) and balanced rotation (day; Fritsch et al. 1994; Trier and Davis 2002; Davis and Trier 2002). Serial MCVs, those persisting through more than one diurnal cycle,

* The National Center for Atmospheric Research is sponsored by the National Science Foundation.

Corresponding author address: Christopher A. Davis, National Center for Atmospheric Research, P.O. Box 3000, Boulder, CO 80307.
E-mail: cdavis@ucar.edu

DOI: 10.1175/MWR3398.1

produce widespread swaths of heavy rainfall as they travel eastward over North America (Fritsch et al. 1994) or Asia (Wang et al. 1993) or westward over Africa (Berry and Thorncroft 2005).

In general, it is believed that these vortices form within the stratiform region of MCSs where mesoscale convergence occurs into a hydrostatically induced pressure minimum. Thus, the earth's rotation is the primary source of a vertical component of vorticity (Hertenstein and Schubert 1991; Skamarock et al. 1994). However, vortex tilting can make a substantial contribution (Brandes 1990; Zhang 1992) and can produce mesoscale vortices even in the absence of background rotation (Davis and Weisman 1994).

The observing facilities for BAMEX and some preliminary results are summarized in Davis et al. (2004). Three aircraft were utilized in BAMEX—two WP-3D Orion aircraft, each equipped with dual-scanning tail Doppler radars, and a Lear jet (model 35A) leased from Weather Modification Incorporated (WMI). For mature MCVs with only scattered precipitation, the P-3s were not deployed. The data were then collected exclusively from the Lear jet and also by mobile GPS-Loran Atmospheric Sounding Systems (MGLASS) on the ground. There were three MGLASS units, each capable of launching soundings every 60–90 min. The Lear jet could deploy dropsondes at a maximum rate of 7 h^{-1}. Given the typical speed of the jet (150–200 m s^{-1}), the resulting spacing of the soundings was about 80–100 km. Thus, mesoscale structure of the MCVs could be resolved, especially using time–space correction of the soundings from multiple flight tracks across the vortex (Davis et al. 2004).

Some structural information has been obtained in past studies of MCVs, through ground-based or airborne Doppler winds, or composites of operational soundings and wind profilers. Studies using soundings or wind profilers, including Menard and Fritsch (1989), Fritsch et al. (1994), Bartels et al. (1997), and Knievel and Johnson (2002), generally underresolved the vortex and only through the compositing of soundings over a multiday life cycle did Fritsch et al. (1994) obtain a three-dimensional, smoothed depiction of the MCV. In the radar-based studies (Brandes 1990; Johnson and Bartels (1992); Scott and Rutledge 1995; Yu et al. 1999; Reasor et al. 2005), the primary shortcoming was a lack of thermodynamic data. The radar studies also tended to focus on developing vortices with horizontal scales on the order of 50 km that may have been line-end vortices (Weisman 1993). Some of these may have evolved into MCVs, but the later evolution of these developing circulations was largely unaddressed. The present study adds to previous work by providing both kinematic and thermodynamic data that resolve the MCV, including tilts and asymmetries, and by depicting its environment.

The present paper focuses on the observed kinematic and thermodynamic structure of five mature MCVs. In a companion paper (Trier and Davis 2007, hereafter Part II of this study), we will analyze how variations in vertical and horizontal motions influence convection within the circulation of the same five MCVs. Each vortex originated within an earlier, nocturnal MCS and was observed with varying amounts of rainfall within its circulation several hours after the decay of the parent convection. We will show clear vertical penetration of vorticity into the boundary layer in one case and a suggestion of surface cyclonic circulation in two other cases. We will show that virtual potential temperature perturbations are typically small (1°–2°C) and are nearly balanced, according to a nonlinear-balance diagnosis. The detailed structure of the vortices appears to be significantly affected by vertical wind shear and the presence or absence of tropopause-based cyclonic and anticyclonic circulation anomalies.

2. Analysis methods

Observations used in the present study include GPS dropsondes, MGLASS, National Oceanic and Atmospheric Administration profiler network wind profilers, reflectivity images from the Weather Surveillance Radar-1988 Doppler network, National Weather Service (NWS) soundings, surface observations, and operational analyses obtained from the National Centers for Environmental Prediction (NCEP). The available soundings and profiler observations for each case, centered in time with respect to each flight of the WMI Lear jet, were manually quality-controlled to remove visually spurious observations. These most often consisted of "spikes" in both wind components, with the wind observation deviating sharply at a single point. Thermodynamic data were generally considered good. There are some known problems with dropsonde temperatures, including wetting of the instruments upon the descent through cloud and precipitation layers. This can lead to spurious layers of high static stability. However, inspection of the raw soundings revealed that this was not a serious problem unless soundings descended through deep cloud layers characteristic of mature convection.

Based on an initial estimate of motion of the vortex derived from cloud and radar animations, and later corrected with the sounding and profiler observations, all data were time–space corrected to approximately the

mean time of the dropsonde deployment period (average of the time of the first and last drops). Because the data were typically collected over a 3-h period, the corresponding maximum temporal shift of the data was about 1.5 h. Given a typical translation speed of 10 m s^{-1} or less, this resulted in a maximum displacement of about 70 km. Characteristic time and space displacements were roughly half these values. These typical time and space corrections were generally smaller than the characteristic time and space scales of the vortices themselves. Given a vortex of radius $R \sim 100$ km, the radius of maximum tangential wind $V \sim 10$ m s^{-1}, and denoting $\Delta u \sim 10$ m s^{-1} as the vertical shear across the depth of the vortex, the relevant time scales are (i) the inertial period, $2\pi R/V$ (about 18 h), and (ii) the shear time scale, $2R/\Delta u$ (about 6 h).[1]

An analysis of wind derivatives is performed using the triangle method (Bellamy 1949), wherein collections of three wind profiles, from any source, form the three vertices, and derivatives are calculated using line integrals around the perimeter. The advantages of the triangle approach for estimating derivatives over traditional techniques are quantified in Spencer and Doswell (2001). Stokes' (Gauss's) theorem allows one to evaluate vorticity (divergence) using the line integral of the wind component along (normal to) each leg. The triangle method assumes that the average wind along each leg is well represented by the average of the wind at the vertices bounding each leg. Hence, the variation of wind is linear along each side of the triangle. As a result, relative vorticity (hereafter simply vorticity) and horizontal divergence are assumed constant within each triangle.

Two sets of triangle restrictions are imposed. The more restrictive conditions require a minimum acute angle of 0.4 radians, maximum side length of 250 km, and area between 1000 and 30 000 km^2. The less restrictive conditions require a minimum acuteness of 0.25 radians, maximum side length of 300 km, and area between 1000 and 40 000 km^2. The more restrictive constraints on triangle geometry are used unless data near the periphery of the MCV are consistently excluded from triangles. Then the less restrictive conditions are invoked.

Our triangle selection method differs from that used in previous studies (e.g., Ceselski and Sapp 1975; Menard and Fritsch 1989), in which, within a given scan radius from original data locations, triangles were selected with optimal size and obliqueness characteristics, or studies (e.g., Spencer and Doswell 2001) that determined a set of independent triangles (i.e., ones that have no area overlap). Although more discriminating, these methods do not necessarily yield a unique set of "optimal" triangles.

In this paper, we will only consider vorticity derived from triangles of observations, but Part II reports results of kinematic vertical motion derived from vertically integrating divergence profiles valid at the centroid of triangles. To analyze vorticity, we superpose a regular grid on the set of triangles generated that meet the above criteria. We assume that, consistent with the assumption of linear variation of wind along the triangle sides, the constant vorticity so obtained is valid everywhere within the triangle, not just at the centroid. The vorticity values within all triangles that overlap a given grid point are averaged to obtain an analyzed value. The grid spacing is 0.25° latitude, or about 28 km, in all cases. The analysis method preserves exactly the area integral of vorticity, while allowing greater detail where more observations are concentrated and less detail where observations are sparser. The analysis method also requires no assumptions common to objective analysis, such as a radius of influence of an observation.

In addition, an estimate of the confidence in the analysis is obtained by computing the standard deviation among all vorticity values averaged at a given grid point. In this way, the overlap of the triangles is used to highlight regions of inconsistency in the analysis. In the limit that all triangles are the same size, the standard deviation could be treated as an estimate of analysis error. In the inevitable case of inhomogeneously distributed data, the analysis in regions of large standard deviation should be interpreted with caution, and perhaps ignored. In general, we find that a useful discriminator of analysis consistency is whether the standard deviation remains below one-half of the maximum of vorticity in the field. Normalizing by the maximum vorticity accounts for the dependence of vorticity variations on the vortex intensity. The factor of 1/2 is a compromise between the background noise value (between 1/4 and 1/3 of the maximum value) and the maximum standard deviation in the analysis domain.

The most computationally involved analysis is the determination of balance. Results appear in section 4b, but here we describe the procedure used. Having obtained an analysis of relative vorticity on pressure levels (with a 10-hPa spacing), we invert this vorticity to obtain a nondivergent streamfunction ψ from $\nabla^2\psi = \zeta$, where ζ is the relative vorticity and the Laplacian op-

[1] The factor of $2R$ represents the minimum displacement for which the top and bottom of an ideal cylindrical vortex do not overlap.

erator is two-dimensional (x and y). The domain contains 61 points (1500 km) in each horizontal direction, and a homogeneous Dirichlet condition is applied on the boundary. The solution ψ is then used to solve the nonlinear balance equation (Charney 1955),

$$\nabla^2\phi = f_0\nabla^2\psi + 2\left[\frac{\partial^2\psi}{\partial x^2}\frac{\partial^2\psi}{\partial y^2} - \left(\frac{\partial^2\psi}{\partial x\partial y}\right)^2\right], \qquad (1)$$

subject to homogeneous lateral boundaries on ψ and the geopotential ϕ. In deriving (1), all terms involving horizontal divergence have been neglected from the divergence equation. Because the motions considered are mesoscale, we have also neglected the variation of the Coriolis parameter f_0 in (1) (Haltiner and Williams 1980, p. 61).

The hydrostatic equation is then used to compute a virtual potential temperature using $\partial\phi/\partial\pi = -\theta_v$, where π is the Exner function $C_p(p/p_0)^{(R_d/C_p)}$ and θ_v the virtual potential temperature. The resulting virtual potential temperature is averaged over 100 hPa layers from 900 to 300 hPa, resulting in values at 850 hPa, 750 hPa, etc. Because there is no guarantee of consistency from level to level using (1), there can be considerable noise in the hydrostatically derived profiles with a 10-hPa vertical increment. The averaged fields are well behaved, however, and still retain enough resolution to see the basic thermal structure.

To compare balanced and observed profiles of θ_v, we first horizontally interpolate the balanced, layer-averaged virtual potential temperature to the sounding locations (Fig. 1) using a nearest-point scheme. We average the observed virtual potential temperature over the same 100-hPa deep layers over which we averaged the balanced θ_v. Next, we divide the vortex-centered domain into four quadrants: northeast, northwest, southwest, and southeast (Fig. 1). Each quadrant is divided into 2 range bins—radius $r < R_{\max}$ and $R_{\max} < r < 300$ km—where $R_{\max}$ varies between 100 and 150 km (Table 1). All soundings within a given quadrant and range bin are averaged to produce a single, mean sounding, and the resulting mean soundings for each quadrant within a given range bin are then averaged to produce a sounding representing either the inner structure ($r < R_{\max}$) or the outer structure ($R_{\max} < r < 300$ km). The perturbation virtual potential temperature, θ'_v, profile, representing the portion of the virtual potential temperature field attributed to the MCV, is then the outer mean sounding subtracted from the inner mean sounding. The agreement between balanced and observed perturbation virtual potential temperature profiles will determine the degree of balance.

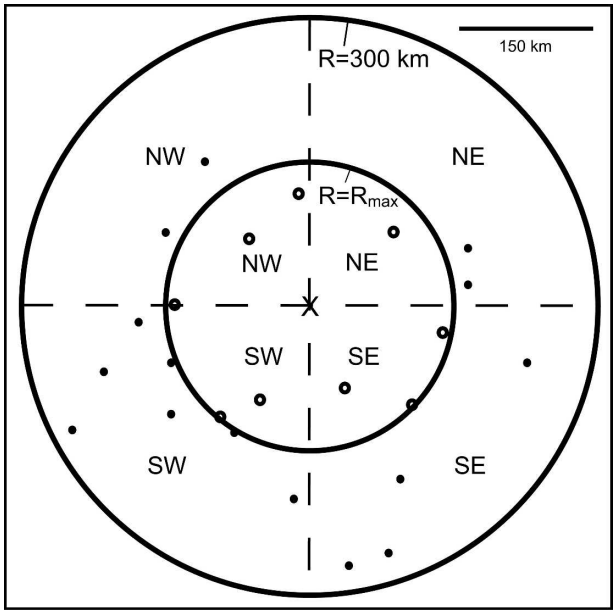

FIG. 1. Illustration of quadrant definitions used in assessment of balance. Small open and closed circles indicate vortex-relative sounding locations for IOP 8 (11 Jun 2003). Open circles are located at radii less than the radius of maximum wind ($R_{\max}$); filled circles are located between $R_{\max}$ and 300-km radius. Dashed lines separate quadrants. The X denotes the center of the MCV.

Averaging within quadrants is important for removing biases due to the spatial distribution of soundings. In Fig. 1, it is apparent that the number of soundings within a given quadrant (and radial bin) ranges from one to seven, so the inhomogeneity of the data distribution is an important issue. This is particularly true if large-scale gradients are present.

The balance computation does not include vorticity outside a distance of about 300 km from the vortex center, even though the computational domain is 1500 km on a side; hence, the synoptic-scale structures that are not part of the vortex should not be present in the balanced solution. Such synoptic-scale structures *are* included in the observed soundings, but the subtraction of the outer from the inner mean sounding will remove most of this large-scale influence.

For an isolated MCV, there can be an induced temperature perturbation even outside $R_{\max}$; hence, subtracting the outer region may also remove some of the temperature anomaly of the vortex. Thus, the temperature anomalies computed herein may be slightly weaker than would be obtained with different definitions of a "far-field" thermodynamic state. The observed and balanced virtual temperatures are treated identically, however, so that the comparison of the two is valid nonetheless.

TABLE 1. Properties of each of the MCVs examined. Date is in month/day/hour (mm/dd/hhhh) format and specifies the middle of the IOP, i.e., the valid time of time–space-corrected observations. Translation speed and direction (west–east movement is 270°) are used to time–space correct soundings and profilers. The maximum tangential wind V_m is estimated from Fig. 7; R_m is the radius of the maximum tangential wind (also estimated from Fig. 7); vertical shear in the layers from 1 to 4 km and 1 to 8 km AGL is computed from data presented in Fig. 8; MCV duration is estimated from radar and satellite animations and is determined by beginning and ending times when rotation is discernable, or from wind profilers indicating a vortex passage by a wind shift in the lower midtroposphere; origin is determined subjectively from radar composites; surface penetration is assessed based on Figs. 6 and 7.

IOP	1	4	5	8	15
Date (mm/dd/hhhh)	05/24/1930	06/02/1500	06/05/2120	06/11/1730	06/29/2050
Translation speed ($m\ s^{-1}$)/direction (°)	15/280	10/257	0/NA	13/250	6/270
V_m ($m\ s^{-1}$)	13	15	12	15	10
R_m (km)	100	150	100	150	100
Shear 1–4 km ($m\ s^{-1}$)	12	14	12	2	8
Shear 1–8 km ($m\ s^{-1}$)	14	27	32	5	13
Duration (h)	12	12+	12	60+	15+
Origin	MCS	Hybrid	MCS	MCS (2 nights)	Multi-MCS
Surface penetration	Uncertain	Weak	Weak or none	Strong	Weak

3. Antecedent conditions

a. Synoptic scale

Maps of 500-hPa height, vorticity, and 850-hPa wind valid at 0000 UTC prior to each observed case (Fig. 2) reveal a wide variation in the antecedent synoptic-scale and mesoscale conditions. Only Intensive Observing Periods (IOPs) 4 and 8 (2 and 11 June, respectively; see Table 1) had a cyclonic vorticity maximum upshear relative to where convection later organized. The vorticity maximum in the IOP 4 case had temporal continuity, moving across the western United States on 1 June. The strength of this precursor made IOP 4 a hybrid case, by which we mean that cyclonic vorticity production within an MCS was entangled with vorticity production through synoptic-scale cyclone dynamics. It is well known that extratropical cyclones produce localized anomalies of vorticity and potential vorticity in the lower and midtroposphere through diabatic heating, and these can structurally resemble MCVs (Emanuel et al. 1987; Montgomery and Farrell 1991). We use the term "synoptic scale" even though the precursor disturbance had a half wavelength of less than 1000 km. The scale of the precursor was still roughly a factor of 3 larger than the ensuing MCS and MCV, but there was nonetheless some ambiguity in defining an MCV in IOP 4. The precursor in IOP 8 was the remnant of the MCV that formed within convection on the previous night. The other cases featured generally straight midtropospheric flow from the west-northwest at 500 hPa in the vicinity of developing convection.

The flow pattern at 850 hPa exhibited southeasterly winds within the region where the nocturnal MCS would form in each case except IOP 8 (Fig. 2d), wherein a cyclonic circulation was evident over the Oklahoma–Kansas border, with southerly and southwesterly flow over the region where convection developed. Based on an examination of 0000 UTC National Weather Service soundings,[2] the vertical wind shear prior to the nocturnal MCS was at least 15 $m\ s^{-1}$ between 900 and 600 hPa (about 1 and 4 km MSL) in all cases except IOP 8, wherein the vertical shear was about 12 $m\ s^{-1}$. Conditional instability, as represented by convective available potential energy (CAPE) derived from the same soundings used to estimate vertical shear, was roughly 500 J kg^{-1} on 24 May and 2 June, nearly 1000 J kg^{-1} on 5 June, and nearly 2000 J kg^{-1} on 11 and 29 June.

b. Antecedent MCSs

A snapshot of each of the MCSs leading to the MCVs analyzed below appears in Fig. 3. These times are chosen to represent the mature convective systems during the time when the MCV was forming, based on signatures of mesoscale rotation in animations of composite radar reflectivity images. All developing vortices at this time appeared within extensive regions of stratiform precipitation, consistent with observational studies (e.g., Bartels and Maddox 1991).

The MCS that produced the MCV observed in IOP 1 (24 May) was actually the second of 2 distinct convective lines. The first organized over southern Nebraska during the evening of 24 May, then propagated rapidly southeast, leaving an apparent vortex signature in radar reflectivity (white "X" in Fig. 3a), first noted around 0900 UTC. A second convective line developed near

[2] The specific soundings used were (i) North Platte, Nebraska, on 24 May, (ii) Dodge City, Kansas, on 2 June, (iii) Amarillo, Texas, on 5 June, (iv) Norman, Oklahoma, on 11 June, and (v) Dodge City, Kansas, on 29 June.

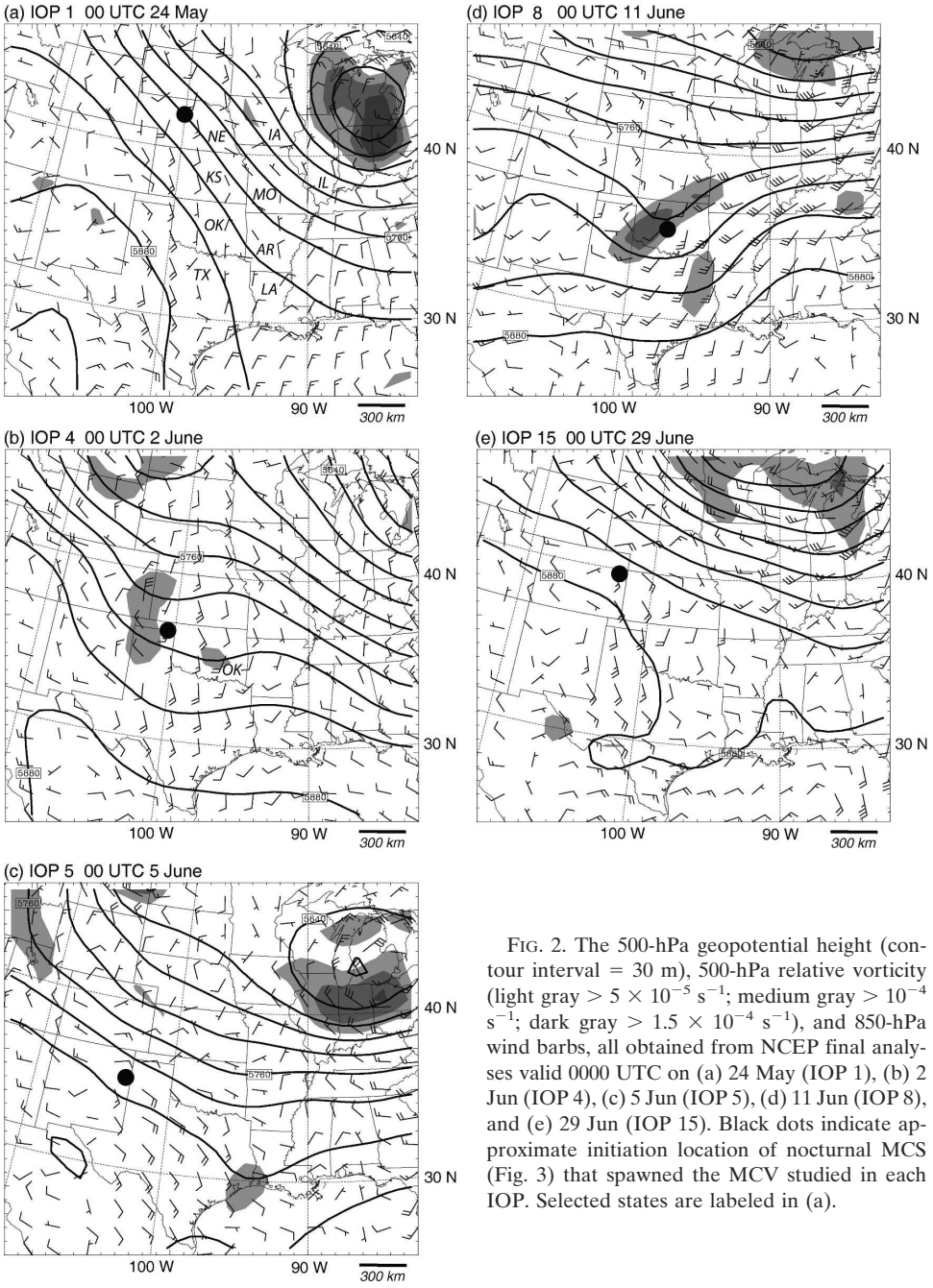

FIG. 2. The 500-hPa geopotential height (contour interval = 30 m), 500-hPa relative vorticity (light gray $> 5 \times 10^{-5}$ s^{-1}; medium gray $> 10^{-4}$ s^{-1}; dark gray $> 1.5 \times 10^{-4}$ s^{-1}), and 850-hPa wind barbs, all obtained from NCEP final analyses valid 0000 UTC on (a) 24 May (IOP 1), (b) 2 Jun (IOP 4), (c) 5 Jun (IOP 5), (d) 11 Jun (IOP 8), and (e) 29 Jun (IOP 15). Black dots indicate approximate initiation location of nocturnal MCS (Fig. 3) that spawned the MCV studied in each IOP. Selected states are labeled in (a).

the Kansas–Oklahoma border around 1200 UTC, then propagated southeastward at nearly 20 m s^{-1} into eastern Oklahoma (Fig. 4a), dissipating around 1600 UTC. The remnant vortex sampled during IOP 1 moved nearly due eastward into Arkansas, where dropsonde observations began around 1700 UTC.

The precursor MCS to the MCV of IOP 4 (2 June) featured weaker and shorter-lived convection (Figs. 3b, 4b) than in IOP 1, but the precipitation region was widespread, presumably owing in part to the influence of the upper-level precursor trough (Fig. 2b). Rotation of the rain shield to the north of the most intense convection began even earlier than the time shown and persisted well into the morning of 2 June. Observations of the MCV began around 1400 UTC over extreme eastern Kansas and western Missouri.

Prior to IOP 5 (5 June), an intense MCS developed over western Texas and matured into a classical asym-

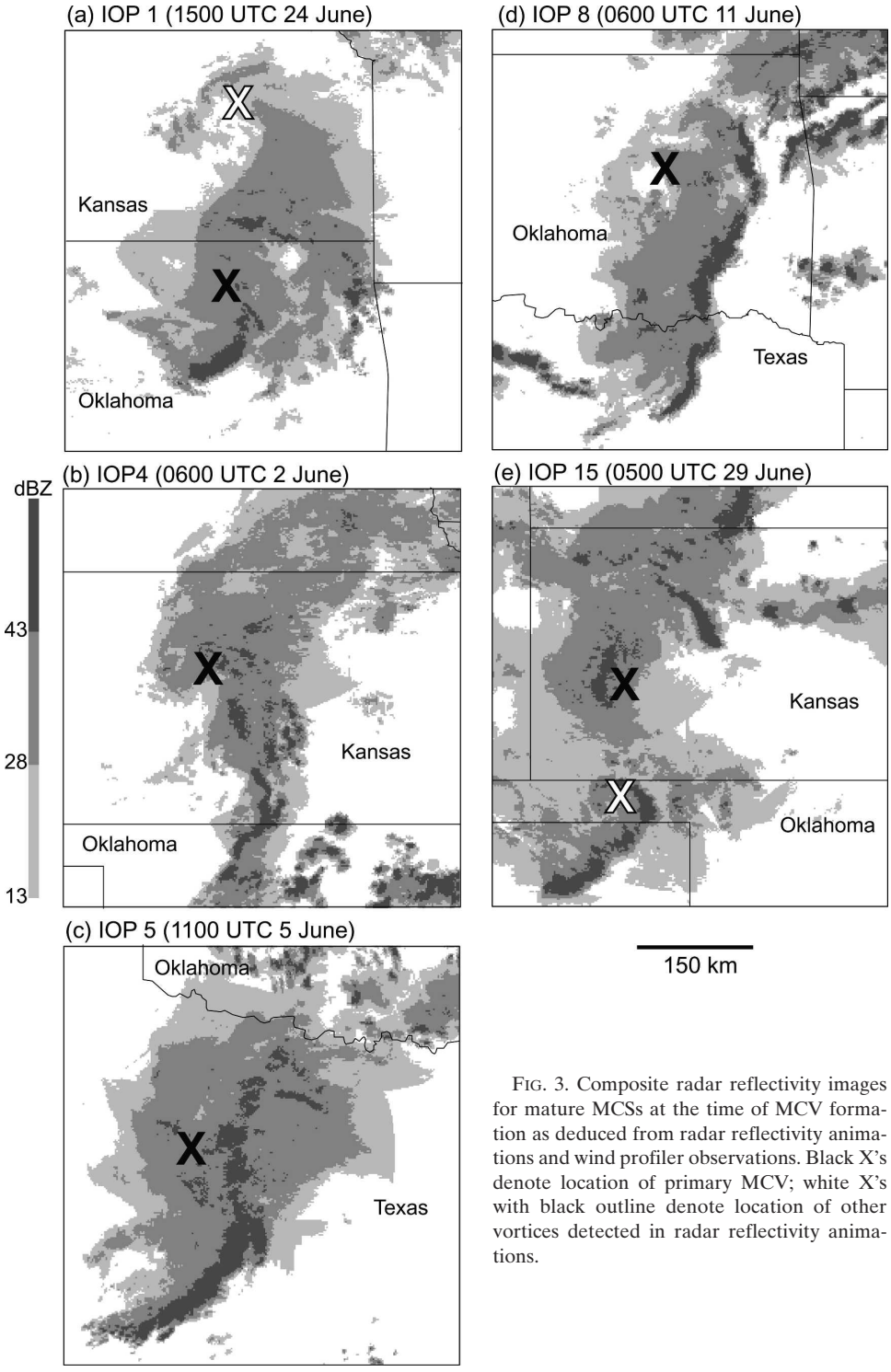

FIG. 3. Composite radar reflectivity images for mature MCSs at the time of MCV formation as deduced from radar reflectivity animations and wind profiler observations. Black X's denote location of primary MCV; white X's with black outline denote location of other vortices detected in radar reflectivity animations.

metric MCS (Houze et al. 1990) by 0800 UTC (Fig. 3c). The leading line of convection propagated southeastward while the remnant MCV moved nearly due eastward during the morning of 5 June (Fig. 4c). Dropsonde observations began around 2000 UTC during the following afternoon.

The precursors to the MCV of IOP 8 are described in Galarneau and Bosart (2005) as nocturnal MCSs occur-

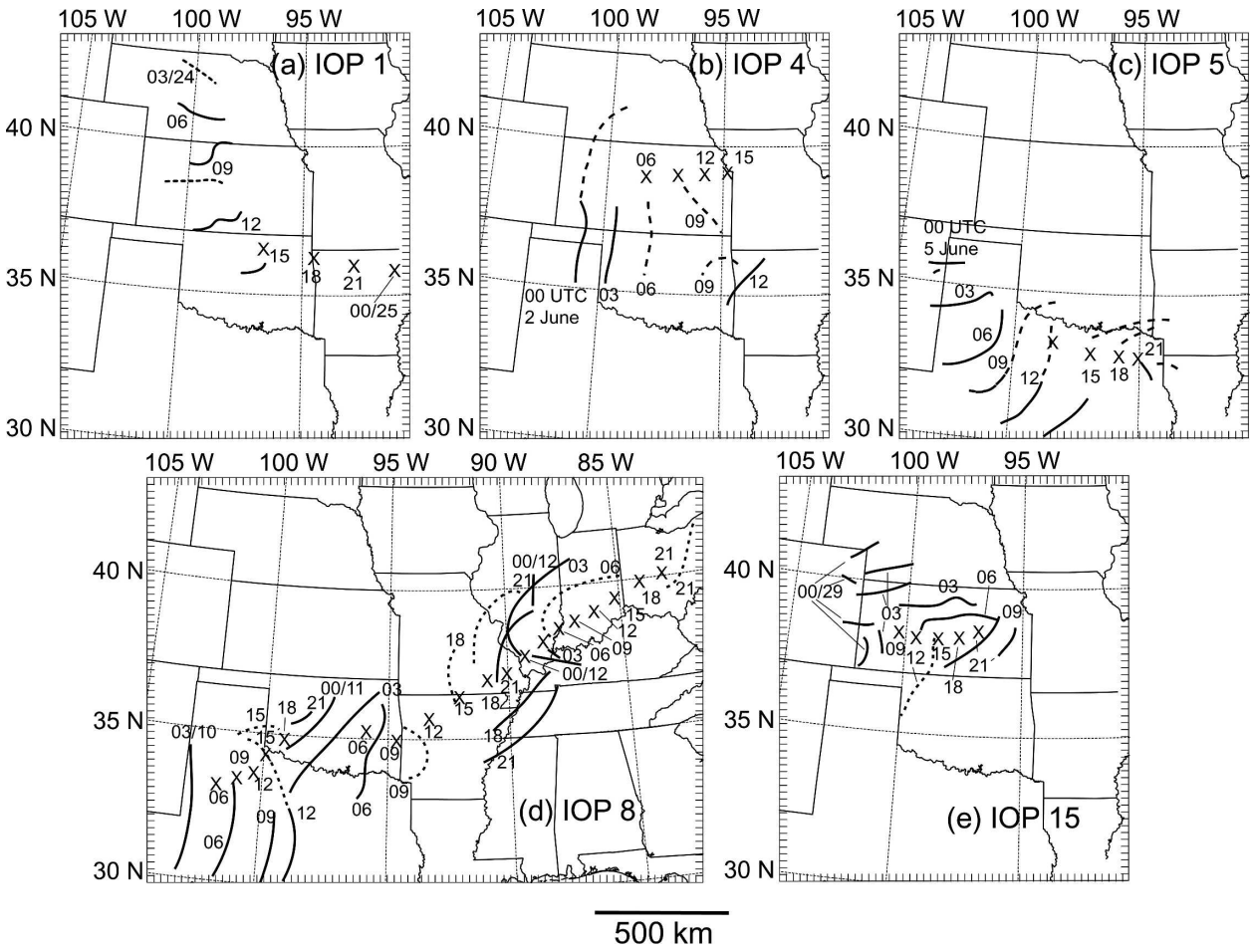

FIG. 4. Isochrones of leading convective lines (solid = solid line of reflectivity > 40 dBZ, dashed = broken line with cells > 40 dBZ) and positions of MCVs (X's), all at 3-h intervals for each IOP. Two-digit numerical labels refer to time (UTC), while the first symbol of the day is marked by both hour and day (hh/dd).

ring on successive nights, both triggered by a shortwave disturbance embedded within the subtropical jet. The first MCS formed over eastern New Mexico on the evening of 9 June and produced an MCV over western Texas early on 10 June (Fig. 4d). This vortex moved northeastward over western Oklahoma by the afternoon of 10 June and is depicted as a southwest–northeast-tilted trough at 500 hPa in Fig. 2d. New convection developed approximately 150 km northwest of Norman, Oklahoma, around 0000 UTC 11 June (Fig. 4d) and evolved into another asymmetric MCS overnight. Strong horizontal rotation became evident to the west of the leading line of convection by 1000 UTC. This vortex subsequently moved along the Arkansas–Missouri border and was sampled by dropsondes beginning at 1600 UTC 11 June.

The MCV sampled during IOP 15 arose during a complex evolution of convection featuring as many as four simultaneous, distinct convective lines (Figs. 3e, 4e). The vortex apparently formed within a widespread region of moderate-to-heavy rainfall (Fig. 3e) not clearly connected to a line of thunderstorms at this time (0500 UTC). By 1000 UTC, the rotation of the remnant echoes of this region became evident as the MCV moved into central Kansas. Sampling of the MCV began around 2000 UTC.

4. Mesoscale convective vortices

a. Structure

Two perspectives of the structure of the five MCVs will be presented in this section: plan views and cross sections. Plan views on the 800-hPa surface appear in Fig. 5. These analyses were manually constructed using all the available wind profiler, dropsonde, and sounding observations. All data were time–space corrected based

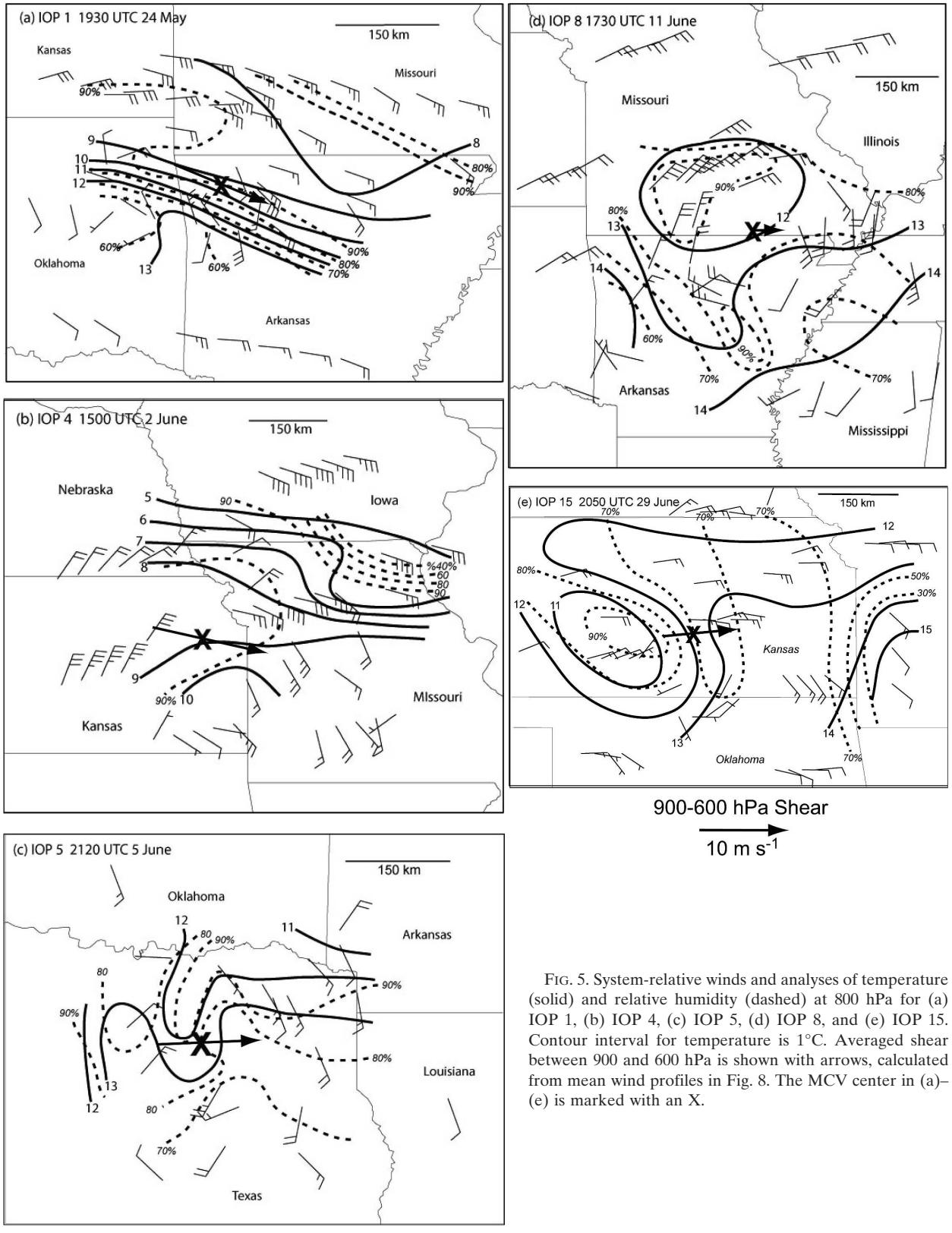

FIG. 5. System-relative winds and analyses of temperature (solid) and relative humidity (dashed) at 800 hPa for (a) IOP 1, (b) IOP 4, (c) IOP 5, (d) IOP 8, and (e) IOP 15. Contour interval for temperature is 1°C. Averaged shear between 900 and 600 hPa is shown with arrows, calculated from mean wind profiles in Fig. 8. The MCV center in (a)–(e) is marked with an X.

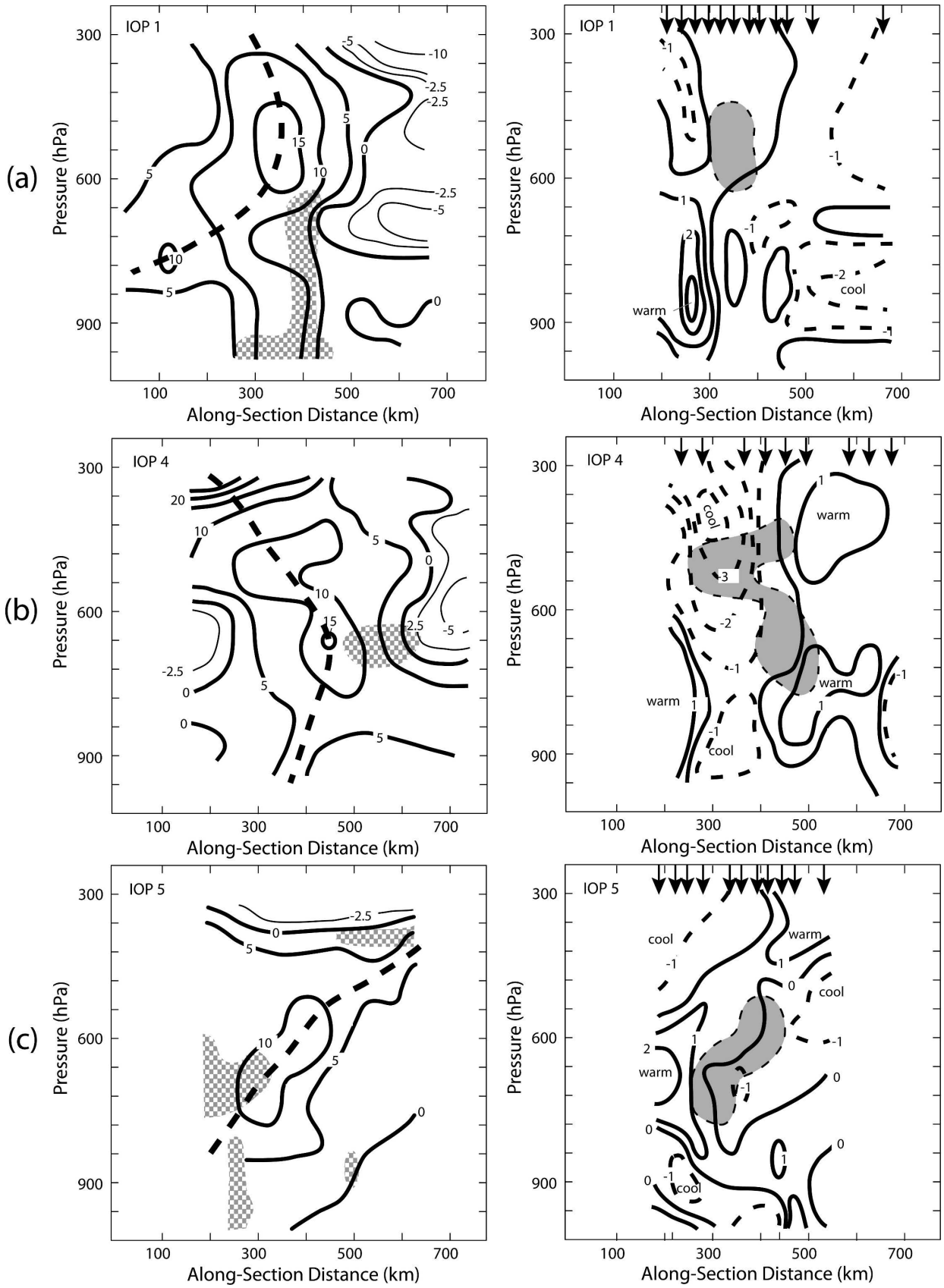
(a)
IOP 1
Pressure (hPa)
Along-Section Distance (km)
warm
cool
(b)
IOP 4
Pressure (hPa)
Along-Section Distance (km)
warm
cool
(c)
IOP 5
Pressure (hPa)
Along-Section Distance (km)
warm
cool

FIG. 6.

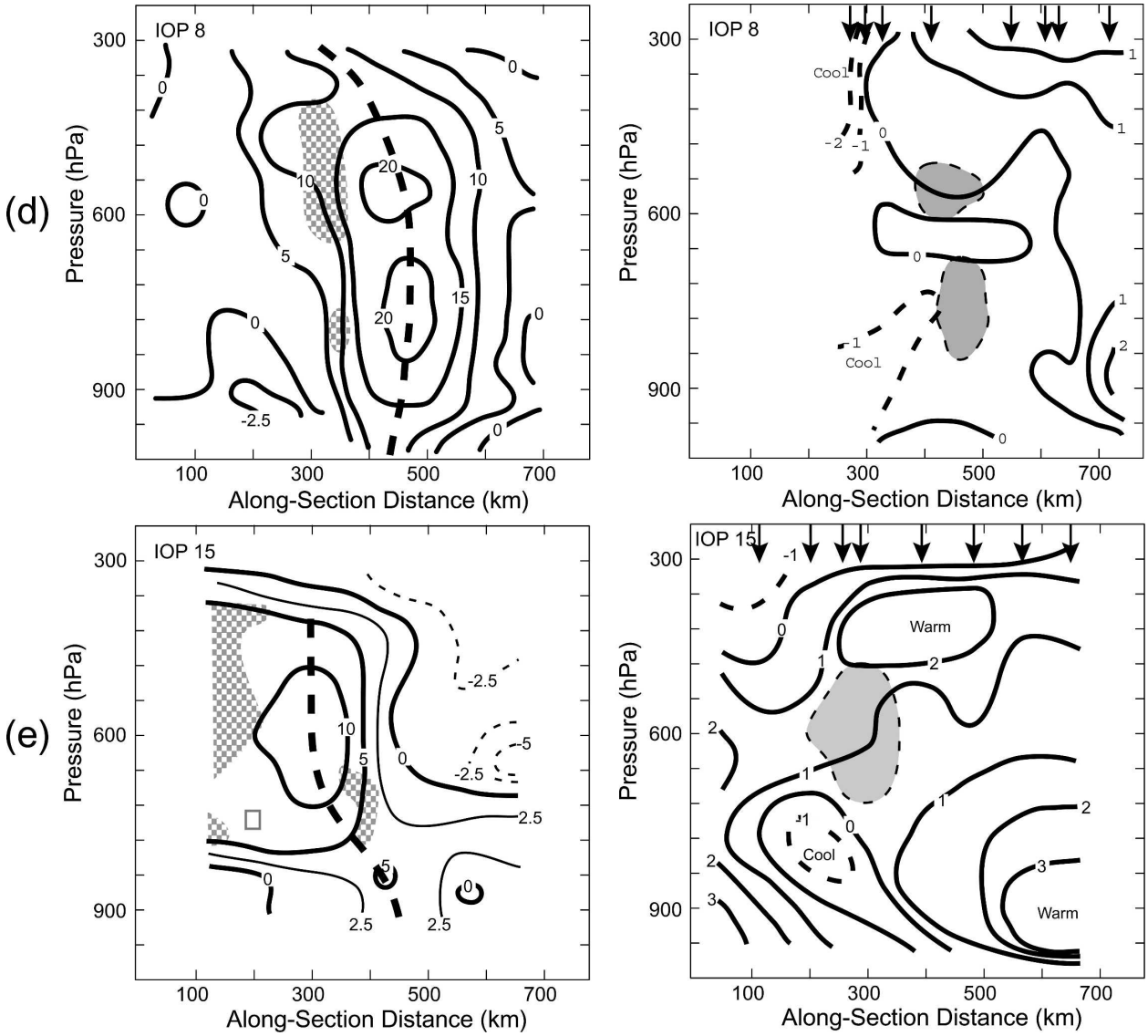

FIG. 6. (*Continued*) East–west vertical cross sections through the center of each of the five MCVs: (a) IOP 1, 1930 UTC 24 May; (b) IOP 4, 1500 UTC 2 Jun; (c) IOP 5, 2120 UTC 5 Jun; (d) IOP 8, 1730 UTC 11 Jun; and (e) IOP 15, 2050 UTC 29 Jun. For each IOP, the left panel shows relative vorticity, contoured in intervals of 5×10^{-5} s^{-1} (except 2.5 for negative values). Gray stippling indicates regions where the standard deviation of the vorticity exceeds half the maximum value. Heavy dashed line in left panels denotes vortex axis. Right panels show virtual potential temperature deviations (see text), contour interval 1 K, dashed for negative values. Also shown are arrows indicating the location of soundings projected into the cross section. Gray shading shows relative vorticity, in units of 10^{-4} s^{-1}, greater than (a) 1.5, (b) 1.0, (c) 1.0, (d) 2.0, and (e) 1.0.

on the translation velocities appearing in Table 1. Soundings from the National Weather Service were included if they were collected within 2 h of the central time of the analysis. In only two cases, IOPs 5 and 15, were NWS soundings incorporated. A maximum of five hourly profiler observations were also included in each case, except in IOP 1, where data from two successive flights were merged. Profilers are evident in Fig. 5 as collections of wind barbs along a straight line, separated equally and by a distance typically less than 30 km.

From Fig. 5 analyses at 800 hPa, it is clear that significant variation in structure exists among the cases. Strong baroclinity was evident in IOPs 1 and 4. Recall that the MCV of IOP 4 was a hybrid case, heavily influenced by a precursor baroclinic cyclone. The IOP 1 MCV was observed immediately after the cessation of a severe bow echo that developed in a high shear environment. Thus, the presence of strong shear surrounding each of these two MCVs was not surprising.

In IOPs 5, 8, and 15, significant east–west tempera-

ture variations were part of the MCV structure, in addition to the systematic north–south temperature variations that also existed. For instance, in IOPs 8 and 15 (Figs. 5d,e), locally cool air was present near but slightly west (IOP 15) or northwest (IOP 8) of the vortex center at this level. System-relative southerly or southeasterly wind and associated warm advection were evident to the east of the vortex center in each case. In Part II, it will be shown that this area of warm advection generally corresponds to mesoscale lifting, and it is in these regions where new convection forms, in accord with the quasi-balanced lifting emphasized in theoretical work (Raymond and Jiang 1990) and diagnosis based on operational model analyses (Trier and Davis 2002).

The location of cool anomalies to the west of the vortex center in IOPs 5 and 15 may result partly from temperature advection in northerly flow behind the vortex, and especially in the case of IOP 15 (Fig. 5e), may mark the location of heavy overnight precipitation and a failure of the boundary layer to develop during the daytime. We note that at 800 hPa in IOPs 8 and 15 (Figs. 5d,e, respectively), the cool anomaly to the west of the vortex weakens markedly as one moves still farther west to where the boundary layer grows deeply during the afternoon.

In 4 cases, the relative humidity at 800 hPa reached a maximum value either within the vortex core or slightly poleward of it (Fig. 5). Only in IOP 15 did the humidity maximum occur to the west of the vortex center, perhaps as a result of heavy precipitation in the area during the previous night. The location of the air with the lowest humidity was more variable, occurring to the southwest of the vortex center in two cases (IOPs 1 and 8; Figs. 5a,d), to the east or northeast in two cases (IOPs 4 and 15; Figs. 5b,e), and to the southeast of the vortex in one case (IOP 5; Fig. 5c). In IOP 8, the dryness probably resulted from strong isentropic downglide. In IOP 1, the dryness could be traced back to the base of a rear-inflow jet (whose existence is confirmed by an MGLASS sounding launched at 1353 UTC; not shown herein) behind the bow echo that spawned the MCV. In the other cases, it appeared that mesoscale variations of water vapor not directly associated with the MCV or its antecedent convection accounted for the location of dry air.

East–west vertical cross sections of relative vorticity (Fig. 6), computed by averaging gridded vorticity (described in section 2) over a 1° latitudinal extent centered on the 600-hPa circulation center, indicate the vertical structure of the vorticity anomalies in each case (left panels). These cross sections are all aligned east–west and within ±20° of the lower-tropospheric vertical shear vector. The approximate axis of maximum cyclonic vorticity at each level is also indicated. To prevent unwarranted extrapolation of the data, the analyses in Figs. 6 and 7 are done by hand.

The vertical structure and intensity of circulation differed substantially among the cases. The vortex depths varied from perhaps 5 km in IOP 5 to 8 km in IOP 8, and the extent of vertical penetration to 900 hPa or below varied highly among the cases. The MCV of IOP 1 (Fig. 6a) appeared to penetrate to the surface, but this part of the analysis was highly uncertain (see stippled region), perhaps because data from two successive Lear jet flights were composited, thus making the stationarity assumption less valid. More certain was the downshear tilt of vorticity, with a secondary vorticity maximum around 750 hPa westward of the midtropospheric maximum by about 200 km. In IOP 4 (Fig. 6b), some penetration to the surface was evident, although this could be related to the synoptic-scale cyclone within which the MCV was embedded. More obvious was the large cyclonic vorticity near and above 300 hPa located to the west of the MCV. This represented the continuation of the shortwave disturbance evident in Fig. 2b. In IOP 5 (Fig. 6c), a sharp tilt of the vortex was apparent, with anticyclonic vorticity evident in the upper troposphere. Little, if any, penetration to the surface was noted here. The MCV of IOP 8 (Fig. 6d) was clearly evident in the boundary layer and at the surface and was the most intense MCV of the five. Little tilt of the vortex was evident, except for an apparent upshear tilt in the upper troposphere due to the proximity of a precursor, tropopause-based disturbance. In IOP 15 (Fig. 6e), the vortex was sharply confined to the midtroposphere with a strong anticyclone aloft and to the east. The existence of an anticyclone immediately to the east of the vortex was characteristic of IOPs 1 and 4 as well. It is possible that this feature existed in the other cases but was outside the analysis domain. There was an upshear tilt of the vortex apparent in the lowest 1.5 km; however, it is likely that the cyclonic vorticity near the surface was tied to a north–south-oriented stationary front (not shown).

The thermal structure of each MCV was analyzed by projecting all soundings within 1° of the axis of the cross section onto the cross-sectional plane (Fig. 6, right panels). To make horizontal and vertical variations of virtual potential temperature comparable, the mean vertical structure of virtual potential temperature averaged over all soundings was subtracted. The systematic meridional temperature gradient (derived from the mean vertical shear over the depth of the vortex, based on mean wind profiles shown in Fig. 8) was accounted for by adding a temperature perturbation $\theta_v' = (\xi - \xi_0)d\Theta_v/d\xi$,

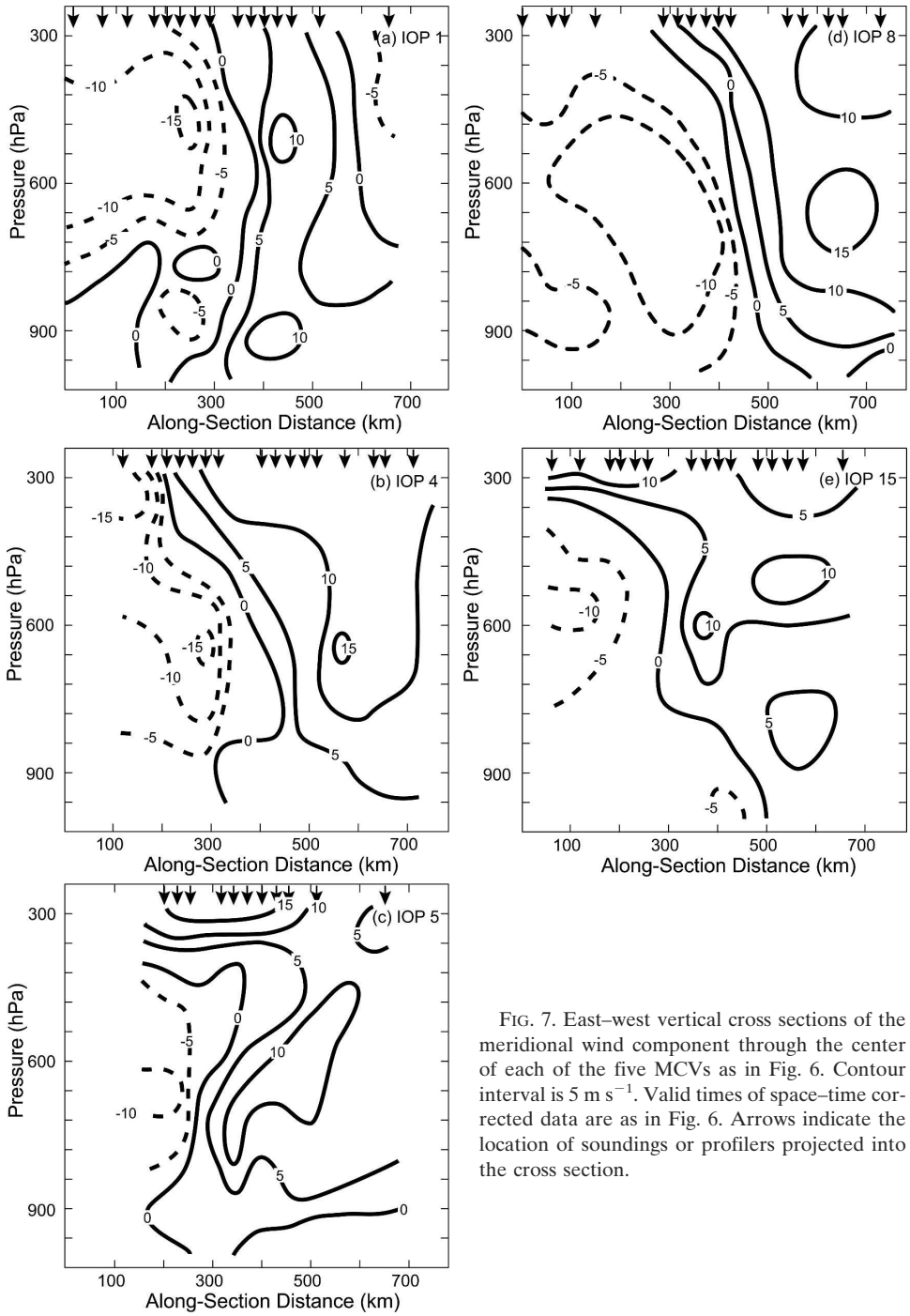

FIG. 7. East–west vertical cross sections of the meridional wind component through the center of each of the five MCVs as in Fig. 6. Contour interval is 5 m s^{-1}. Valid times of space–time corrected data are as in Fig. 6. Arrows indicate the location of soundings or profilers projected into the cross section.

where ξ is latitude and Θ_v is the potential temperature in thermal wind balance with the mean vertical wind shear.

Near the MCV of IOP 1 (Fig. 6a), the virtual potential temperature anomaly field featured a positive anomaly centered at 800 hPa to the west of the MCV center. This area was a remnant of the descending rear inflow from the MCS shown in Fig. 3a. An MGLASS sounding taken at 1353 UTC confirmed the existence of the subsaturated rear-inflow jet in the active bow echo (not shown). This area of warm and relatively dry air persisted several hours after the convection dissipated. Also of note was the lack of cool air directly beneath the MCV except in a shallow layer near 650 hPa. More

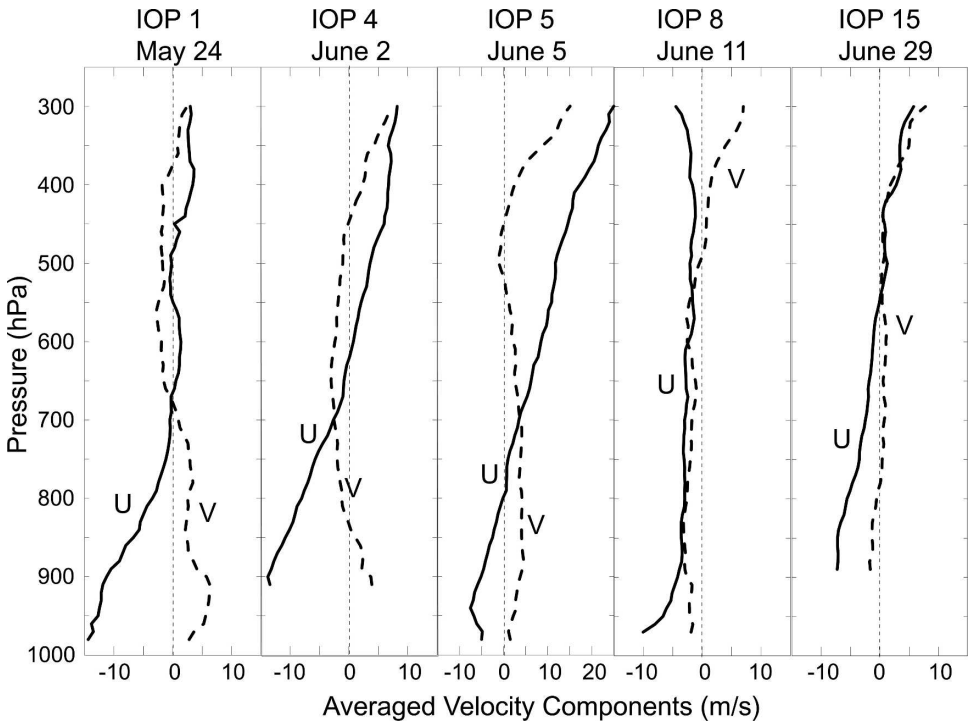

FIG. 8. Mean vertical profiles of zonal (solid) and meridional (dashed) wind components for each MCV IOP.

extensive cool air was found farther east, associated with the southeasterly moist flow and perhaps evaporational cooling from precipitation or simply a systematic gradient of θ_v on the synoptic scale.

The thermal structure in IOP 4 (Fig. 6b) was considerably different from that in IOP 1. An upper-tropospheric warm anomaly was displaced downshear from the midlevel MCV center. The pronounced cool anomaly above 500 hPa was associated with the upper-tropospheric trough, as would be required qualitatively by thermal wind balance. However, this anomaly extended to the surface, and in the lower troposphere was associated with cold advection behind a cold front. Recall that this was the only hybrid case wherein the MCV was superposed on a baroclinic wave structure. The MCV itself may have altered the temperature field given the weak warm anomaly between 900 and 700 hPa immediately to the east of the vortex center, suggesting locally enhanced warm advection. Overall, the lower-tropospheric temperature field was broadly consistent with meridional thermal advection induced by the MCV. Note that the cool anomaly beneath the midtropospheric MCV center was small compared to the lower-tropospheric anomalies on the flanks of the MCV, in contrast to what has been traditionally portrayed as part of MCVs (e.g., Chen and Frank 1993; Fritsch et al. 1994).

In IOP 5 (Fig. 6c), the virtual potential temperature anomalies above 700 hPa were consistent with a strongly tilted vortex wherein the cooler air lay beneath the sloping vorticity maximum and warmer air above. A weak thermal dipole was apparent near 900 hPa, with warmer air to the east and cooler air to the west of the vortex center, but again, with a comparatively small virtual potential temperature anomaly directly beneath the midtropospheric MCV center. The clear tilting of the vortex in this case would dictate that any cool anomaly in the lower troposphere should be located upshear with respect to the midtropospheric MCV center.

The virtual potential temperature anomalies near the MCV of IOP 8 were smaller than in any other case, despite the fact that it was the most intense MCV. A cool anomaly above 500 hPa can be discerned on the western edge of the analysis region associated with the tropopause-based trough located to the west of the vortex. A weak cool anomaly was present beneath and to the west of the midtropospheric vortex center (Fig. 6d). In the lower troposphere, warm air to the east of the vortex was present, as also indicated in Fig. 6d.

The virtual potential temperature anomalies in IOP 15 more resembled the classical structure associated with MCVs. There was a warm anomaly above the midtropospheric center, displaced slightly to the east,

consistent with the formation of an upper-tropospheric anticyclone (Fig. 6e). The thermal structure of IOP 15 featured the most pronounced signature of cool air beneath the vortex of any case.[3] This cool anomaly was shifted slightly to the west of the vortex, perhaps indicating some effect of meridional advection by the MCV, as in IOPs 4 and 5. However, as noted earlier, it could also reflect a lack of boundary layer growth during the day in response to wet ground resulting from heavy precipitation during the previous evening. There was warm air well to the east of the MCV that was also dry (Fig. 6e) and hence remained free of secondary convection. This warm, dry air was already in place when convection developed several hundred kilometers to the west during the previous evening.

Further comparison of the cases is facilitated by examining the meridional wind component in the same cross section as shown in Fig. 7. For each case, the analysis of wind proceeded analogously to that of the temperature in Fig. 7. All soundings and profilers within 1° latitude from the axis of the cross section were projected onto the section and manually analyzed. While the temperatures were corrected for the systematic north–south baroclinity, no correction of the meridional wind was performed.

The meridional wind (Fig. 7) was broadly consistent with the vorticity (by definition) and with the virtual temperature perturbation field (as implied by the thermal wind balance). The maximum wind occurred near 600 hPa in all cases except IOP 1, wherein it was found just below 500 hPa. The horizontal scale of the vortices was estimated to be half the distance between positive and negative wind maxima in Fig. 7. As summarized in Table 1, the horizontal scale varied between 100 km (IOPs 1, 5, and 15) and about 150 km (IOPs 4 and 8).

In IOP 1, a second circulation center is apparent near 900 hPa, although as was seen in Fig. 6a, this part of the analysis should be interpreted cautiously. This vortex was the only case with continuous heavy stratiform rainfall in its center (see Part II), so it is possible that the cyclonic vorticity structure at low levels is the result of recent diabatic heating and cooling. It is also apparent in IOP 1 that the midtropospheric vortex trailed increasingly westward below 600 hPa and appeared distinct from the circulation center lower down. In Part II it will be shown that there were rainbands oriented southeast–northwest to the east of the midtropospheric vortex center. A preliminary Doppler radar analysis performed by W.-C. Lee, M. Bell, and R. Wakimoto (National Center for Atmospheric Research, 2004, personal communication) reveals a cyclonic wind shift associated with these bands at altitudes as low as 1 km AGL. These transient features likely contribute uncertainty to the analysis of vorticity in this case (Fig. 6a).

In IOPs 4, 5, and 15 (Figs. 7b,c,e, respectively), east–west-oriented baroclinic zones with frontal characteristics appear to obscure the signature of the vortex at the surface. It will be shown in Part II that there are southerlies at the surface to the southeast of the MCV center, but it is unclear whether these southerlies are directly linked to the MCV. In particular, the dipole of meridional wind in IOP 15 (Fig. 7e) located within 200 hPa of the surface to the east of the MCV is consistent with a pronounced west–east thermal gradient in the boundary layer that is not obviously related to the MCV.

The results of the foregoing analysis can be put into context by considering the mean wind profiles in each case. These profiles (Fig. 8) were constructed by first averaging zonal and meridional winds at each pressure level among all soundings in a given azimuthal quadrant. Then the mean profiles for each quadrant were averaged to obtain the mean wind profile. By weighting observations unevenly in this manner, quadrant partitioning helped alleviate biases due to the uneven distribution of observations. The largest vertical shear in the mid- and upper troposphere occurred during IOP 5 and was consistent with the large downshear tilt of the vortex in the upper troposphere. The largest shear in the lower troposphere occurred in IOP 1, and in that case, there was also considerable downshear tilt of the vortex below 600 hPa (Fig. 6a). Some tilt was also apparent in IOP 4, if one notes the weak vorticity maximum at 900 hPa displaced roughly 100 km to the west of the vortex center at 700 hPa.

The weak vertical shear that accompanies the MCV of IOP 8 is less than 5 m s^{-1} between 900 and 400 hPa. This is consistent with the relative lack of vortex tilt and likely allows an extended lifetime of this vortex (Fig. 4) because of the modest straining force applied. The vertical structure of the vortex in IOP 15 is somewhat at odds with the shear. A slightly upshear tilted structure is apparent below 800 hPa. It is likely that the vorticity in the boundary layer is part of a weak front due, in part, to the cool air near the surface beneath the western edge of the midtropospheric MCV center. The appearance of cyclonic vorticity in the boundary layer is likely not a direct downward extension of the MCV.

The horizontal vorticity structure of the different MCVs can be summarized by considering horizontal (constant pressure) profiles of vorticity. To preserve

[3] The overall bias of the virtual temperature field to positive anomalies in this case is a result of the method used to compute a perturbation and is not dynamically meaningful. Thus, the magnitude of the cool anomaly should be inferred by the surrounding gradients rather than by the minimum value.

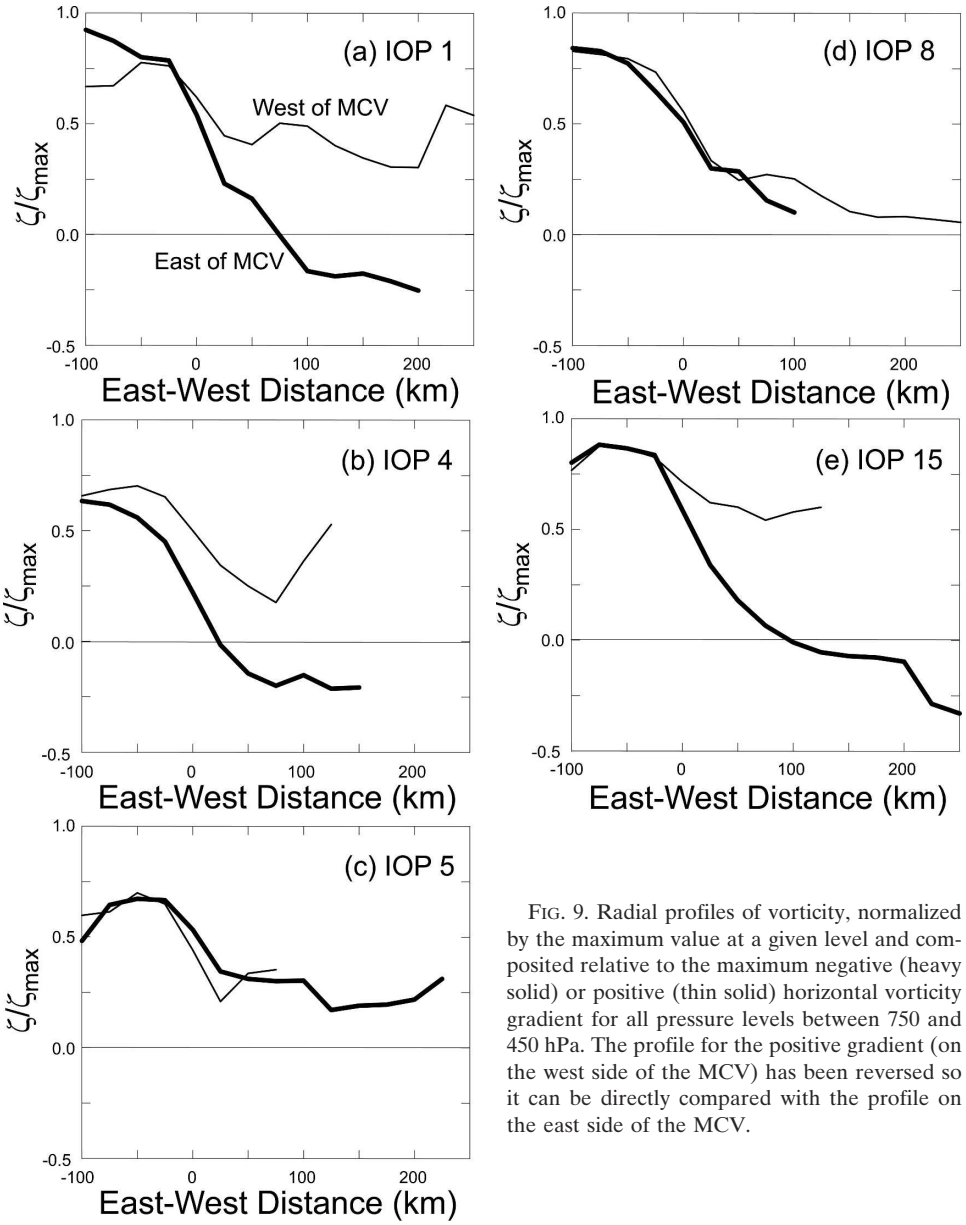

FIG. 9. Radial profiles of vorticity, normalized by the maximum value at a given level and composited relative to the maximum negative (heavy solid) or positive (thin solid) horizontal vorticity gradient for all pressure levels between 750 and 450 hPa. The profile for the positive gradient (on the west side of the MCV) has been reversed so it can be directly compared with the profile on the east side of the MCV.

the true vorticity gradient, we construct vertically averaged horizontal profiles for each case with the horizontal coordinate centered on the maximum horizontal vorticity gradient at each altitude included in the average. It proves too difficult to construct meaningful azimuthal mean gradients owing to the inhomogeneous distributions of data, so we confine the analysis to the plane of the cross sections shown in Figs. 6, 7, that is, to the east–west direction (which is nearly shear parallel in all cases). To more easily compare profiles from different cases, we normalize each profile by the maximum vorticity of the MCV in the same east–west plane (Fig. 6). The gradient-relative profiles between 750 and 450 hPa are averaged to produce Fig. 9.

The radial vorticity profiles for IOPs 1, 4, and 15 show a marked asymmetry between the downshear (east) and upshear (west) sides, with the downshear side containing a substantially sharper gradient, transitioning to negative relative vorticity. The formation of a downshear, midtropospheric anticyclone is apparent and constitutes a new finding. Previously, the anticyclone was thought to be confined to the upper troposphere only. Data in IOP 8 do not extend far enough downshear to determine whether the vorticity changes sign. The MCV of IOP 5 does not exhibit a downshear anticyclone, and it is unknown if this is related to the pronounced background shear and MCV tilt.

In IOP 8, the vorticity profile is nearly symmetric and

contains an extensive "skirt," or modest gradient out to at least a 250-km radius, and this could be a factor in the longevity of the MCV. A similar radial profile of potential vorticity was found in the theoretical work by Schecter et al. (2002) to induce damping of shear-induced asymmetries on a vortex. Such waves will be damped through critical line dynamics, provided that there exists a negative radial gradient of relative vorticity at the critical radius for waves on the vortex. Although the vertical shear across the MCV in IOP 8 is weak (Fig. 8), there is still enough shear that one ought to see a tilt after many hours of evolution if no alignment process is active. However, we did not see any tilt in the available observations. Thus, while IOP 8 is the only case in which adiabatic vortex realignment is possible, we have no direct evidence for its occurrence as in idealized models of vortices in modest shear (Jones 1995; Trier et al. 2000a; Reasor et al. 2004).

b. Balance

A key issue is whether MCVs are balanced structures, that is, whether the wind and temperature fields obey a prescribed, slowly evolving relationship to each other. The importance of balance, described in classic papers such as Hoskins et al. 1985, is that these so-called slow modes, arising from high-frequency modes such as deep, moist convection in the present case, efficiently interact with surrounding potential vorticity structures, modifying jets or surface fronts and initiating Rossby waves that travel thousands of kilometers. The existence of balance implies that on time scales of a day or longer, it is only the diabatic redistribution of potential vorticity that is an important outcome of convection. The details, however important for local weather within the convection system, are otherwise not relevant. Balance is critical for weather prediction several days hence, not only because slow modes are usually more predictable but also because incomplete observations better constrain the initial state of a forecast model if there is a well-defined statistical relation between them. Balance summarizes this statistical relation and is clearly a key element of data assimilation.

Given observations of wind, for instance (from wind profilers, cloud-drift winds, or other sources), it is important to correctly infer the temperature perturbation associated with the vortex. In view of the somewhat surprising temperature anomaly patterns near the MCVs, where cool anomalies were weak below the center of the circulations, the question of whether such structures are balanced naturally arises. Consistency with thermal wind balance was noted in Figs. 6 and 7 for each case, but herein we will show more quantitative evidence of balance.

Previous studies based either directly on numerical simulations or on analyses derived partly from numerical models have found MCVs to be highly balanced systems, especially when deep convection is not extensive (Davis and Weisman 1994; Olsson and Cotton 1997; Trier and Davis 2002). However, the only study that explicitly addresses the "instantaneous" balance solely from observations is Knievel et al. (2004). Their conclusion was that the temperature structure retrieved from the winds departed substantially from a state of gradient wind balance (similar to the nonlinear balance constraint considered herein). Their study was for a single case, with data coverage far more limited than in the present study, and the cause of imbalance was not determined.

To address whether the mature MCVs observed during BAMEX represented dynamically balanced structures, we focus on the relative abundance of wind information available in this study and use the unprecedented sounding network of BAMEX to assess agreement with the thermodynamic conditions inferred from the nonlinear balance Eq. (1). While the traditional approach is to compute Rossby–Ertel potential vorticity (PV) and solve the fully coupled inversion equations (e.g., Hoskins et al. 1985; Davis and Emanuel 1991), practical considerations require another approach. First, since we wish to compare observed and balanced virtual potential temperature profiles, the specification of the potential temperature on upper and lower boundaries, as is usually done for PV inversion, will bias our result in favor of balance by definition. Second, there are more wind data than temperature data, given the profiler network. Hence, the domain over which PV can be calculated is confined relative to the domain over which the relative vorticity can be computed.

The approach for computing balanced virtual potential temperature perturbations, given winds, is outlined in section 2. Results for four cases are presented in Fig. 10 as profiles of balanced and observed differences between inner and outer layer-averaged virtual potential temperature. Recall that inner and outer averages are obtained by averaging soundings within each of the four quadrants, and then averaging the quadrants. Balanced virtual potential temperatures are interpolated to the same sounding locations and the same averaging process is performed for consistency. The distribution of data in IOP 4 was deemed too asymmetric in the outer region to allow a reasonable assessment of temperature anomalies; hence that case is not included here.

Comparison of balanced and observed profiles strongly suggests that the MCVs are indeed balanced

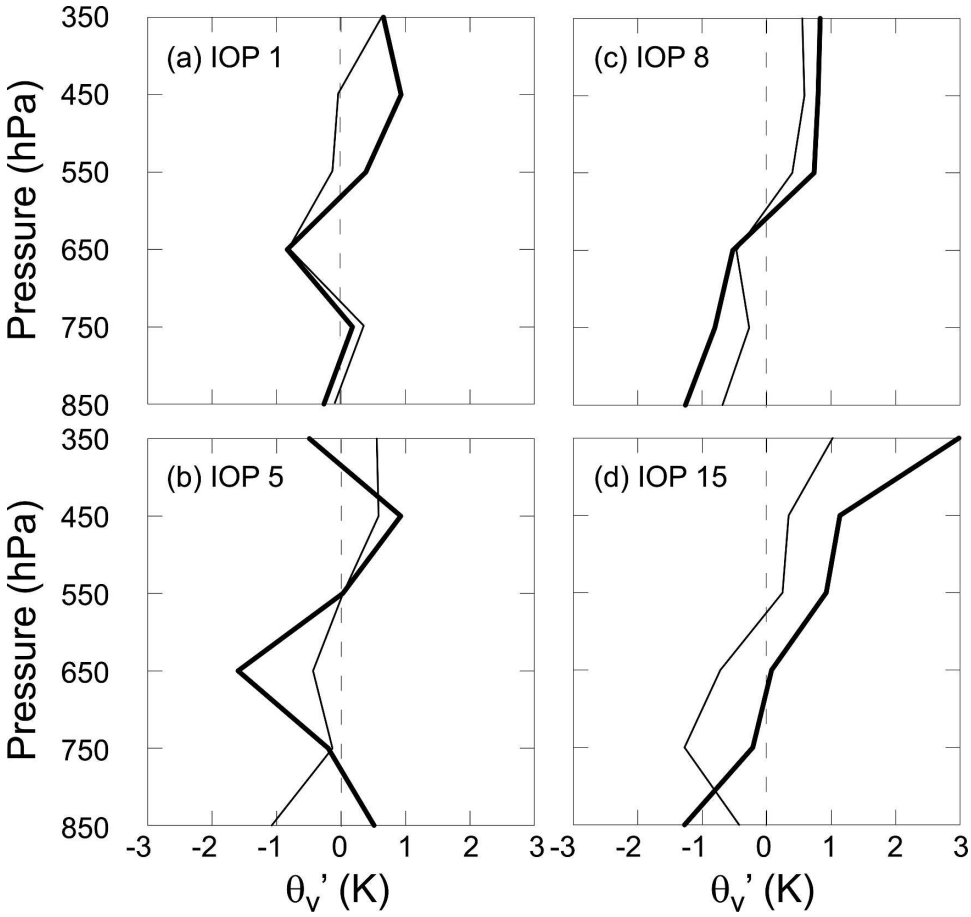

FIG. 10. Perturbation virtual potential temperature (K) profiles from observations (heavy lines) and balanced calculation (thin lines). See text for details. Temperatures represent vertical averages over 100-hPa layers centered on the pressure values shown. Perturbations represent the difference between profiles at sounding locations within the radius of maximum wind and profiles outside the radius of maximum wind.

circulations, at least above the planetary boundary layer and within the limitations of the available data. Furthermore, the balance appears most evident in the cases that were best sampled (IOPs 1 and 8), suggesting that previous attempts to deduce balance from observations used datasets that may have been insufficient. Although models or model-based analyses have shown MCVs to be well balanced, this is the first demonstration of balance purely from observations. Thus, the relative absence of cool air directly beneath the midtropospheric (~600 hPa) MCV center in each case of the sample does not appear to be an imbalance, rather it appears to be a limitation of the simple conceptual model of the structure of a mature MCV. The reasons for the absence of extensive cool air beneath the midtropospheric center could be the (i) vertical tilt of the vortex, (ii) horizontal temperature advection due to the vortex itself, (iii) diabatic heating of the lowest levels during the daytime, and (iv) physical lowering of the PV center of the vortex so that its structure is relatively invariant with height in the lower troposphere. The third process above would usually result in unbalanced thermal anomalies; hence it is not a candidate for IOPs 1 and 8. The apparent imbalance at 850 hPa during IOP 5 may be due to influences of the growing afternoon boundary layer, but data limitations preclude a firm conclusion on this issue. The final process was apparent in IOP 8, wherein the MCV penetrated to the surface in association with a vorticity maximum (and likely PV maximum as well) below 700 hPa.

5. Summary and conclusions

Five mature mesoscale convective vortices (MCVs) were sampled by dropsondes, mobile soundings, wind profilers, and NWS soundings during BAMEX. This

article has focused on the structure of the mature vortices using sounding and wind profiler observations of unprecedented spatial resolution. In Part II, we will concentrate on how MCVs influence the environment of deep convection.

Each of the five MCVs could be traced back to rotation evident within a region of stratiform precipitation associated with a mature, nocturnal MCS. In three of the five cases (IOPs 1, 5, and 15), negligible midtropospheric cyclonic vorticity was present in operational analyses prior to the formation of the MCS. These MCVs therefore arose entirely within preceding MCSs. In two other cases (IOPs 4 and 8), significant cyclonic vorticity existed in the mid- and upper troposphere prior to the formation of the nocturnal MCS that produced the vortex. In IOP 4, the antecedent structure was a subsynoptic-scale frontal cyclone; hence this case was termed a hybrid (MCS and MCV dynamics coupled with cyclone dynamics). In IOP 8, the preexisting circulation in the midtroposphere was the remnants of the MCV left from convection during the previous diurnal cycle (1.5 days prior to IOP 8). This case represented the only MCV lasting multiple days observed during BAMEX.

Horizontal analyses of wind and temperature revealed lower-tropospheric temperature advection and associated isotherm deflections resembling those in baroclinic waves, but here on scales of 200–300 km (the range of vortex diameters). The relative humidity above the boundary layer generally maximized within or slightly poleward of the vortex core. Although trajectories could not be computed, we hypothesize this region to represent the maximum upward displacement for air parcels originating in the lower troposphere.

Vertical cross sections showed that each vortex maximized in cyclonic circulation between about 550 and 600 hPa, and also revealed a previously unreported midtropospheric anticyclone located downshear from 3 of the MCVs. The eastward tilt of the vortices with height was in accord with the mean shear acting upon the MCV in three of the five cases. In IOP 15, wherein weak westerly shear was present between the surface and 600 hPa (the height of maximum MCV circulation), the tilt in the lowest 2 km was upshear. This upshear tilt may not have been part of the MCV but instead part of a weak north–south-oriented surface front to the east of the vortex that existed prior to the MCV. In IOP 4, the upshear tilt was indicative of a growing synoptic-scale baroclinic cyclone. The tilt of the MCV in IOP 8 was not detectable, consistent with the very weak shear in that case. However, given the longevity of this MCV (at least 6 h prior to our observations), the observed shear of 3–4 m s^{-1} across the depth of the vortex should have produced an observable spatial displacement of 50–100 km between the lower- and midtropospheric vorticity centers. Such a tilt would have been resolved in our data, but since no such tilt was observed, we conclude that the vortex was resilient, as in the definition of Schecter et al. (2002).

Vertical penetration of MCVs into the boundary layer was clear in only one case (IOP 8). Cyclonic vorticity at the surface was suggested in each of the other cases; however, it was unclear to what extent this vorticity was inextricably linked to the MCV in those four cases. What was clear was that *no* case exhibited a surface anticyclone. The IOP 8 and 15 vortices occurred in relatively weak vertical shear, whereas IOPs 1 and 5 were characterized by strong shear. The IOP 4 MCV was embedded in strong shear but was also part of a larger-scale cyclone, so the surface circulation could be attributed to the synoptic-scale cyclone, perhaps contracting to mesoscale because of frontogenesis and diabatic processes. Given that the cool anomaly directly beneath the midtropospheric MCV center did not exceed 2°C in any case, and in particular, was not weaker in cases that penetrated into the boundary layer, it appears that the removal of the cold dome is not the key factor determining vertical penetration, at least not during the daytime following MCV formation.

It appears that the penetration of an MCV to the surface is related to the vertical shear over the lowest few kilometers. The MCVs of IOPs 1 and 5, in particular, show clear evidence of strongly tilted vortices and neither circulation penetrated to the surface. In IOP 15, a case of moderate shear, penetration is questionable. In IOP 8, the shear is weak and the vortex penetrates strongly. In IOP 4, the shear is strong, but the penetration issue is complicated by synoptic-scale cyclogenesis. From the point of view of the "action at a distance" paradigm of vertical penetration, wherein the local rotation allows an enhanced Rossby penetration depth so that a midtropospheric PV maximum can alter the surface winds (Rogers and Fritsch 2001), shear in lower layers should not matter. It appears, however, that vertical penetration requires the formation of a secondary PV maximum in the lower troposphere, as seen here in IOP 8 and as noted by Davis and Trier (2002), as well as theorized in the context of tropical cyclogenesis by Montgomery et al. (2006). From this perspective, shear is a key factor because it strains the PV, leaving the lower-tropospheric portion of the vortex upshear from the midtropospheric part. From a PV superposition perspective, the sheared vortex, more distributed in space than an erect vortex, induces a weaker horizontal

circulation locally. This is true at all altitudes, but especially at the surface.

The relative abundance of wind and thermodynamic data allowed us to assess the dynamical balance of the MCVs better than in any previous study. In general, we found a high degree of nonlinear balance, especially in cases where the data better sampled the MCV structure. This balanced nature is particularly significant given the observed relative absence of cool air directly beneath the midtropospheric centers of the MCVs, contrasting with a previously well-accepted conceptual aspect of MCVs believed to be consistent with thermal and gradient wind balance. As a practical matter, the balanced nature of MCVs should enhance the ability of assimilation schemes such as three-dimensional variational assimilation (3DVAR) to adequately represent their structure in model initialization provided there are nearly simultaneous observations that resolve the gross features of the vortex.

Acknowledgments. The authors thank Dr. Chris Snyder of NCAR, two anonymous reviewers, and Dr. Rich Moore of ETH, Zürich, for their helpful comments on the manuscript. The authors also thank the BAMEX dropsonde coordinators, David Ahijevych, George Bryan, and Jason Knievel (NCAR), Diana Bartels (NOAA/Forecast Systems Laboratory, now the Global Systems Division), Richard James (the Pennsylvania State University), Dan Hawblitzel (Texas A&M University), and Susan van den Heever (Colorado State University), whose outstanding efforts were critical to the collection of the data used in this study. We also acknowledge the skillful operation of the Lear jet by Weather Modification Incorporated and also acknowledge many of the staff from the Earth Observing Laboratory of NCAR who were responsible for MGLASS and dropsonde operation. We also thank Dr. Stephan Nelson of the National Science Foundation for his support of the Lear jet for BAMEX.

REFERENCES

Bartels, D. L., and R. A. Maddox, 1991: Midlevel cyclonic vortices generated by mesoscale convective systems. *Mon. Wea. Rev.,* **119,** 104–118.

——, J. M. Brown, and E. I. Tollerud, 1997: Structure of a midtropospheric vortex induced by a mesoscale convective system. *Mon. Wea. Rev.,* **125,** 193–211.

Bellamy, J. C., 1949: Objective calculations of divergence, vertical velocity and vorticity. *Bull. Amer. Meteor. Soc.,* **30,** 45–49.

Berry, G. J., and C. Thorncroft, 2005: Case study of an intense African easterly wave. *Mon. Wea. Rev.,* **133,** 752–766.

Brandes, E. A., 1990: Evolution and structure of the 6–7 May 1985 mesoscale convective system and associated vortex. *Mon. Wea. Rev.,* **118,** 109–127; Corrigendum, **118,** 990.

Ceselski, B. F., and L. L. Sapp, 1975: Objective wind field analysis using line integrals. *Mon. Wea. Rev.,* **103,** 89–100.

Charney, J. G., 1955: The use of primitive equations of motion in numerical prediction. *Tellus,* **7,** 22–26.

Chen, S. S., and W. M. Frank, 1993: A numerical study of the genesis of extratropical convective mesovortices. Part I: Evolution and dynamics. *J. Atmos. Sci.,* **50,** 2401–2426.

Davis, C. A., and K. A. Emanuel, 1991: Potential vorticity diagnostics of cyclogenesis. *Mon. Wea. Rev.,* **119,** 1929–1953.

——, and M. L. Weisman, 1994: Balanced dynamics of mesoscale vortices produced in simulated convective systems. *J. Atmos. Sci.,* **51,** 2005–2030.

——, and S. B. Trier, 2002: Cloud-resolving simulations of mesoscale vortex intensification and its effect on a serial mesocale convective system. *Mon. Wea. Rev.,* **130,** 2839–2858.

——, D. A. Ahijevych, and S. B. Trier, 2002: Detection and prediction of warm season midtropospheric vortices by the Rapid Update Cycle. *Mon. Wea. Rev.,* **130,** 24–42.

——, and Coauthors, 2004: The Bow Echo and MCV Experiment: Observations and opportunities. *Bull. Amer. Meteor. Soc.,* **85,** 1075–1093.

Emanuel, K. A., M. Fantini, and A. J. Thorpe, 1987: Baroclinic instability in an environment of small stability to slantwise moist convection. Part I: Two-dimensional models. *J. Atmos. Sci.,* **44,** 1559–1573.

Fritsch, J. M., J. D. Murphy, and J. S. Kain, 1994: Warm core vortex amplification over land. *J. Atmos. Sci.,* **51,** 1780–1807.

Galarneau, T. J., and L. F. Bosart, 2005: An examination of the long-lived MCV of 10–13 June 2003. Preprints, *11th Conf. on Mesoscale Processes,* Albuquerque, NM, Amer. Meteor. Soc., CD-ROM, JP5J.7.

Haltiner, G. J., and R. T. Williams, 1980: *Numerical Prediction and Dynamic Meteorology*. John Wiley and Sons, 477 pp.

Hertenstein, R. F. A., and W. H. Schubert, 1991: Potential vorticity anomalies associated with squall lines. *Mon. Wea. Rev.,* **119,** 1663–1672.

Hoskins, B. J., M. E. McIntyre, and A. W. Robertson, 1985: On the use and significance of isentropic potential vorticity maps. *Quart. J. Roy. Meteor. Soc.,* **111,** 877–946.

Houze, R. A., Jr., B. F. Smull, and P. Dodge, 1990: Mesoscale organization of springtime rainstorms in Oklahoma. *Mon. Wea. Rev.,* **118,** 613–654.

Johnson, R. H., and D. L. Bartels, 1992: Circulations associated with a mature-to-decaying midlatitude mesoscale convective system. Part II: Upper-level features. *Mon. Wea. Rev.,* **120,** 1301–1321.

Jones, S. C., 1995: The evolution of vortices in vertical shear: Initially barotropic vortices. *Quart. J. Roy. Meteor. Soc.,* **121,** 821–851.

Knievel, J. C., and R. H. Johnson, 2002: The kinematics of a midlatitude, continental mesoscale convective system and its mesoscale vortex. *Mon. Wea. Rev.,* **130,** 1749–1770.

——, D. S. Nolan, and J. P. Kossin, 2004: Imbalance in a mesoscale vortex within a midlatitude, continental mesoscale convective system. *J. Atmos. Sci.,* **61,** 1827–1832.

McAnelly, R. L., and W. R. Cotton, 1989: The precipitation life cycle of mesoscale convective complexes over the central United States. *Mon. Wea. Rev.,* **117,** 784–808.

Menard, R. D., and J. M. Fritsch, 1989: A mesoscale convective complex-generated inertially stable warm core vortex. *Mon. Wea. Rev.,* **117,** 1237–1261.

Montgomery, M. T., and B. F. Farrell, 1991: Moist surface fron-

togenesis associated with interior potential vorticity anomalies in a semigeostrophic model. *J. Atmos. Sci.,* **48,** 343–368.

——, M. E. Nicholls, T. A. Cram, and A. B. Saunders, 2006: A vortical hot tower route to tropical cyclogenesis. *J. Atmos. Sci.,* **63,** 355–386.

Olsson, P. Q., and W. R. Cotton, 1997: Balanced and unbalanced circulations in a primitive equation simulation of a midlatitude MCC. Part II: Analysis of balance. *J. Atmos. Sci.,* **54,** 479–497.

Raymond, D. J., and H. Jiang, 1990: A theory for long-lived mesoscale convective systems. *J. Atmos. Sci.,* **47,** 3067–3077.

Reasor, P. D., M. T. Montgomery, and L. D. Grasso, 2004: A new look at the problem of tropical cyclones in vertical shear flow: Vortex resiliency. *J. Atmos. Sci.,* **61,** 3–22.

——, ——, and L. F. Bosart, 2005: Mesoscale observations of the genesis of Hurricane Dolly (1996). *J. Atmos. Sci.,* **62,** 3151–3171.

Rogers, R. F., and J. M. Fritsch, 2001: Surface cyclogenesis from convectively driven amplification of midlevel mesoscale convective vortices. *Mon. Wea. Rev.,* **129,** 605–637.

Schecter, D. A., M. T. Montgomery, and P. D. Reasor, 2002: A theory for the vertical alignment of a quasigeostrophic vortex. *J. Atmos. Sci.,* **59,** 150–168.

Scott, J. D., and S. A. Rutledge, 1995: Doppler radar observations of an asymmetric mesoscale convective system and associated vortex couplet. *Mon. Wea. Rev.,* **123,** 3437–3457.

Skamarock, W. C., M. L. Weisman, and J. B. Klemp, 1994: Three-dimensional evolution of simulated long-lived squall lines. *J. Atmos. Sci.,* **51,** 2563–2584.

Smull, B. F., and R. A. Houze Jr., 1985: A midlatitude squall line with a trailing region of stratiform rain: Radar and satellite observations. *Mon. Wea. Rev.,* **113,** 117–133.

Spencer, P. L., and C. A. Doswell III, 2001: A quantitative comparison between traditional and line integral methods of derivative estimation. *Mon. Wea. Rev.,* **129,** 2538–2554.

Trier, S. B., and C. A. Davis, 2002: Influence of balanced motions on heavy precipitation within a long-lived convectively generated vortex. *Mon. Wea. Rev.,* **130,** 877–899.

——, and ——, 2007: Mesoscale convective vortices observed during BAMEX. Part II: Influences on secondary deep convection. *Mon. Wea. Rev.,* **135,** 2051–2075.

——, ——, and J. D. Tuttle, 2000a: Long-lived mesoconvective vortices and their environment. Part I: Observations from the central United States during the 1998 warm season. *Mon. Wea. Rev.,* **128,** 3376–3395.

——, ——, and W. C. Skamarock, 2000b: Long-lived mesoconvective vortices and their environment. Part II: Induced thermodynamic destabilization in idealized simulations. *Mon. Wea. Rev.,* **128,** 3396–3412.

Wakimoto, R. M., H. V. Murphey, C. A. Davis, and N. T. Atkins, 2006: High winds generated by bow echoes. Part II: The relationship between the mesovortices and damaging straight-line winds. *Mon. Wea. Rev.,* **134,** 2813–2829.

Wang, W., T. T. Warner, and Y.-H. Kuo, 1993: A diabatically driven vortex in the lee of the Tibetan Plateau. *Mon. Wea. Rev.,* **121,** 2542–2561.

Weisman, M. L., 1993: The genesis of severe, long-lived bow echoes. *J. Atmos. Sci.,* **50,** 645–670.

Yu, C.-K., B. J.-D. Jou, and B. F. Smull, 1999: Formative stage of a long-lived mesoscale vortex observed by airborne Doppler radar. *Mon. Wea. Rev.,* **127,** 838–857.

Zhang, D.-L., 1992: The formation of a cooling-induced mesovortex in the trailing stratiform region of a midlatitude squall line. *Mon. Wea. Rev.,* **120,** 2763–2785.

——, and J. M. Fritsch, 1987: Numerical simulation of the meso-β scale structure and evolution of the 1977 Johnstown flood. Part II: Inertially stable warm-core vortex and the mesoscale convective complex. *J. Atmos. Sci.,* **44,** 2593–2612.